J Adv Ceram

Rapid Communication

Sm^{3+} substitution-mediated oxygen vacancy clustering: Theoretical analysis and experimental verification for suppressing low-temperature contraction of $La_2Ce_2O_7$ ceramics

Ruige Sang, Hao Zhang✉, JingJing Liu, Xun He, Jiang Shi, Xun Xu, Shuwang Duo✉

Cite this article: Sang R, Zhang H, Liu J, et al. *J Adv Ceram* 2026, **15**(3): 9221245. https://doi.org/10.26599/JAC.2026.9221245

ABSTRACT: Lanthanum cerate ($La_2Ce_2O_7$, LC) is a promising thermal barrier coating (TBC) candidate with superior thermophysical properties over yttria-stabilized zirconia (YSZ), but its practical application is hindered by low-temperature thermal expansion coefficient (TEC) contraction. Previous studies primarily focused on regulating the oxygen vacancy concentration while neglecting the influences of vacancy distribution. Herein, we employ Sm^{3+} isovalent substitution for La^{3+} to maintain a constant vacancy concentration and isolate the vacancy distribution effects. The optimal composition $(La_{0.8}Sm_{0.2})_2Ce_2O_7$ significantly suppresses low-temperature contraction, reducing the linear shrinkage rate by ~88.5% and increasing the TEC by ~12.56% (to 12.37×10^{-6} K^{-1}) compared with LC (10.99×10^{-6} K^{-1}). Combining density functional theory (DFT) calculations and HR-TEM/AC-STEM characterization, we directly reveal Sm^{3+}-induced oxygen vacancy clustering in LC-based ceramics. The underlying mechanism involves (i) randomly distributed free vacancies inducing contraction via vacancy-phonon coupling and local symmetry breaking; (ii) Sm^{3+} substitution introducing dislocations whose stress fields, together with Sm^{3+}'s higher ionic potential, drive vacancy clustering; (iii) clustering reducing mobile vacancies and restoring lattice order, thereby suppressing contraction. This work confirms that LC's low-temperature contraction is coregulated by vacancy concentration and distribution, complementing existing concentration-modulation strategies.

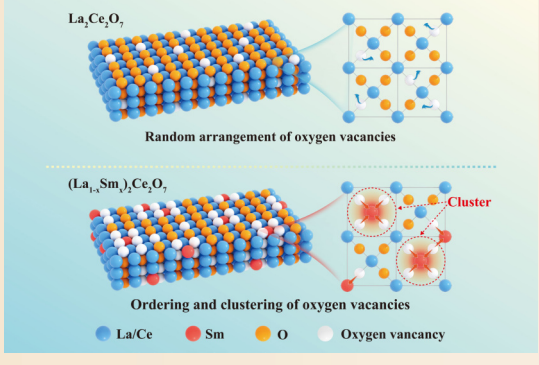

KEYWORDS: thermal barrier coating (TBC); Lanthanum cerate ($La_2Ce_2O_7$); low-temperature contraction; isovalent substitution

1 Introduction

Thermal barrier coatings (TBCs) serve as a critical thermal protective layer for hot-section components of gas turbines and aircraft engines under extremely high temperatures [1–6]. State-of-the-art 6–8 wt% yttria-stabilized zirconia (YSZ) suffers from phase transitions and sintering above 1473 K, driving the search for alternative materials [7–12]. Lanthanum cerate ($La_2Ce_2O_7$, LC), a defective fluorite ceramic containing 1/8 random oxygen vacancies, stands out for its lower thermal conductivity, larger thermal expansion coefficient (TEC), and excellent phase stability up to 1673 K [13,14]. Unfortunately, its low-temperature contraction (i.e., negative thermal expansion) leads to internal stress accumulation and shortens service lifetime, limiting practical applications [13–16].

Previous studies have correlated LC's low-temperature contraction with the oxygen vacancy concentration [13], and high-valent cation substitution (e.g., Ta^{5+}) has been shown to suppress contraction by reducing the vacancy content [15,16]. Nevertheless, these works overlook the potential role of vacancy distribution, leaving a theoretical gap. Although Gd^{3+} substitution was reported to eliminate LC's TEC contraction, direct experimental evidence for the isovalent substitution mechanism remains lacking [17].

To isolate the sole effect of vacancy distribution, we selected Sm_2O_3 as the substituent based on three criteria: the isovalency of Sm^{3+} with La^{3+} (avoiding changes in oxygen vacancy concentration), a matching high melting point (~2598 K, ensuring thermal stability), and a moderate cation radius mismatch (inducing beneficial lattice strain) [16]. This study aims to clarify the influence of vacancy distribution on LC's thermal expansion and verify the proposed "isovalent substitution-vacancy clustering-contraction suppression" mechanism.

2 Experimental

2.1 Sample preparation

$(La_{1-x}Sm_x)_2Ce_2O_7$ (LSC, x = 0, 0.1, 0.2, 0.3, 0.4) powders were

Jiangxi Provincial Key Laboratory of Surface Engineering, Jiangxi Science and Technology Normal University, Nanchang 330013, China.

✉ Corresponding authors. E-mail: H. Zhang, zhanghao@jxstnu.edu.cn, zhangyinghao1985@126.com; S. Duo, swduo@126.com

Received: September 24, 2025; Revised: January 6, 2026; Accepted: January 6, 2026

synthesized via a high-temperature solid-state reaction. High-purity (> 99.9 wt%) La_2O_3, CeO_2, and Sm_2O_3 powders (particle size: 3–6 μm; Changsha Tijo Metal Material Co., Ltd., China) were precalcined at 1273 K for 1 h to remove moisture and impurities. Subsequently, these oxides were mixed in stoichiometric ratios and ball-milled with deionized water and zirconia balls in a polyurethane jar for 24 h. The resulting slurry was dried at 373 K, and the dried mixture was reacted at 1673 K for 12 h to obtain the target LSC powders. The synthesized powders were sieved (100 mesh), uniaxially pressed at 3 MPa for 1 min, and further consolidated by cold isostatic pressing at 250 MPa for 25 min. Finally, the shaped compacts were sintered at 1923 K for 15 h in static air to achieve densification.

2.2 Computational methods

Oxygen vacancy formation energy (E_{vf}) calculations and structural optimizations were performed using density functional theory (DFT), as implemented in the Cambridge sequential total energy package (CASTEP) module of Materials Studio (MS) software, employing the supercell technique [18–20]. The projector-augmented wave (PAW) method was adopted with a cutoff energy of 450 eV. All configurations, CeO_2, LC, and $(La_{0.8}Sm_{0.2})_2Ce_2O_7$ (Fig. S1 in the Electronic Supplementary Material (ESM)), were fully optimized using the generalized gradient approximation (GGA) with the Perdew–Burke–Ernzerhof (PBE) functional. Valence electron configurations were set as $[La]6s^25d^1$, $[O]2s^22p^4$, $[Ce]6s^25d^14f^1$, and $[Sm]6s^24f^6$, with the convergence accuracy set to a maximum force of 5×10^{-2} eV/Å and an energy tolerance of 1.0×10^{-5} eV/atom.

2.3 Characterizations

The crystallographic phase of LSC powders and bulks was analyzed by an X-ray diffractometer (XRD; XRD-6100, Shimadzu, Japan) using Cu-Kα radiation (λ = 0.15406 nm). Data were recorded over a 2θ range of 20°–80° at a scan rate of 4 (°)/min with a step size of 0.02°. Raman spectra for defect structure characterization were acquired using a micro-Raman spectrometer (RTS2, Beijing Zolihan Light Co., Ltd., China) equipped with a 532 nm laser excitation source. Densities and porosity were determined by the Archimedes method in distilled water [21–24]. Linear TECs of LSC bulk samples (dimensions: 25 mm × 7 mm × 1 mm) were measured with a high-temperature dilatometer (HPY-2, Beijing Hengjiu Experimental Equipment Co., Ltd., China) from room temperature to 1750 K at a heating rate of 5 K/min (systematic error within ±0.1%–0.5%). The microstructure and composition of LSC bulks were examined by a field-emission scanning electron microscope (FE-SEM; Sigma, Zeiss, Germany) coupled with an energy-dispersive spectroscope (EDS; Inca, Oxford, UK). Grain size and distribution were statistically evaluated from at least 5 cross-sectional images using ImageJ software. Dislocation defects were characterized by a high-resolution transmission electron microscope (HR-TEM; HT7820, Hitachi, Japan). Atomic-resolution images were obtained using a spherical aberration-corrected scanning transmission electron microscope (AC-STEM; Spectra 300, FEI, USA).

3 Results and discussion

3.1 Crystal structure

Figure 1 shows XRD patterns of LSC bulks together with standard CeO_2 (JCPDS Card No. 34-0394). All patterns resemble the fluorite structure of CeO_2 but exhibit systematic peak shifts toward higher angles with increasing Sm^{3+} content, attributable to the substitution of larger La^{3+} by smaller Sm^{3+} (La^{3+}: 1.16 Å; Sm^{3+}: 1.08 Å; Ce^{4+}: 0.97 Å; data from Ref. [25]). No secondary phases (Sm_2O_3, La_2O_3, or CeO_2) are detected, confirming the formation of a single-phase solid solution. Lattice parameters (Table S1 in the ESM), derived using the Nelson–Riley extrapolation method, decrease linearly with x, further validating successful substitution. The cation radius ratios ($R_{A^{3+}}/R_{B^{4+}}$) (Eq. (1)) for all compositions remain below 1.46 (Table S1 in the ESM), consistent with the defect-fluorite structure [17,26].

$$\frac{R_A}{R_B} = \frac{xR\left(Sm^{3+}\right) + (1-x)R(La^{3+})}{R(Ce^{4+})} \quad (1)$$

3.2 Microstructure and morphology

The sintering temperature (1923 K) is higher than all test temperatures (≤ 1750 K), ensuring structural stability in this study. LC exhibits an average grain size of ~7.18±0.06 μm and a relative density of ~94.9%±0.3% (porosity 5.1%). $(La_{0.8}Sm_{0.2})_2Ce_2O_7$ shows a finer average grain size of ~5.99±0.05 μm and a slightly higher relative density of ~95.4%±0.2% (porosity 4.6%). Both ceramics are crack-free with only sparse closed intergranular pores (Fig. S2 in the ESM), meeting the basic requirements (> 90% density) for reliable thermal expansion measurements [23,24].

3.3 Thermal expansion behavior

Among the LSC series, $(La_{0.8}Sm_{0.2})_2Ce_2O_7$ exhibits the most pronounced suppression of low-temperature contraction and the largest average TEC; it is therefore selected as the representative for detailed analysis. Figure 2(a) illustrates the temperature-dependent linear thermal expansion rates ($\Delta L/L_0$, where ΔL is the line length change of sample, and L_0 is the length of sample at room temperature), while Fig. 2(b) depicts the temperature-dependent TECs. The contraction between 600 and 850 K is reduced by ~88.5% compared with LC (shrinkage rate drops from 12.46% to 1.43%). Concurrently, the maximum TEC increases by ~12.56%, from 10.99×10^{-6} K^{-1} for LC to 12.37×10^{-6} K^{-1} for the Sm-substituted sample. This enhancement is attributed to the decreased electronegativity difference between metal and oxygen upon Sm substitution (the Pauling electronegativities of O, La, and Sm are 3.44, 1.10, and 1.17, respectively), which reduces crystal ionicity and lattice energy, thereby raising the TEC [15,27].

3.4 Oxygen vacancy characteristics

Raman spectroscopy is often used to characterize defect sites in

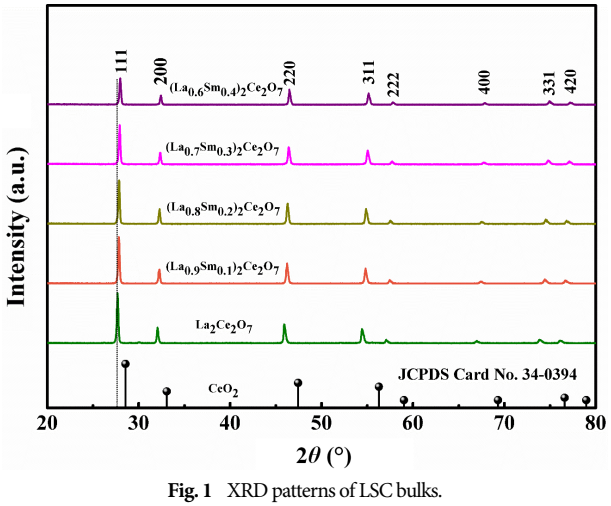

Fig. 1 XRD patterns of LSC bulks.

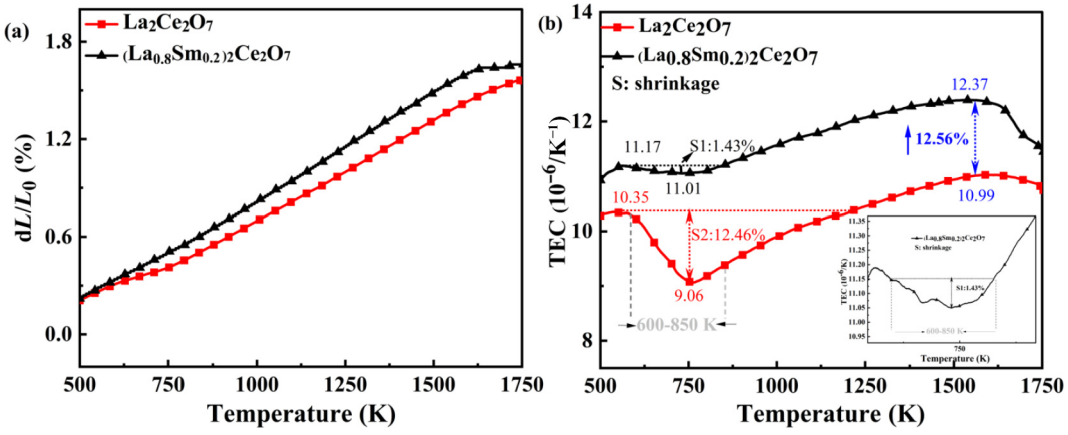

Fig. 2 Thermal expansion behaviors of $(La_{1-x}Sm_x)_2Ce_2O_7$ ($x = 0$, 0.2) bulks.

crystals [16,28,29]. Figure 3 presents Raman spectra of LC and $(La_{0.8}Sm_{0.2})_2Ce_2O_7$. Both samples show the characteristic F_{2g} mode of fluorite at ~460 cm^{-1} (8-coordinate Ce–O vibration) and a defect-related band near 580 cm^{-1} associated with oxygen vacancies. The peak-area ratio (A_{580}/A_{460}), a quantitative indicator of vacancy concentration [16], is nearly identical for the two samples (1.2657 for LC vs. 1.2723 for $(La_{0.8}Sm_{0.2})_2Ce_2O_7$), confirming that the total vacancy content remains unchanged. This validates our design premise that isovalent substitution isolates distribution effects from concentration changes.

Notably, the Raman peaks of $(La_{0.8}Sm_{0.2})_2Ce_2O_7$ are more intense and exhibit a smaller full width at half maximum (FWHM) than those of LC. The enhanced intensity likely arises from lattice ordering due to vacancy clustering, which concentrates scattering signals. The narrower FWHM indicates reduced lattice disorder, consistent with the clustering of previously free vacancies that otherwise perturb Ce–O bond uniformity. These spectroscopic observations align with XRD peak shifts and the ordered structural features later revealed by AC-STEM.

3.5 Vacancy clustering mechanism

HR-TEM analysis reveals Sm^{3+}-induced dislocations along the [200] direction in $(La_{0.8}Sm_{0.2})_2Ce_2O_7$ (Fig. 4(e)). Such dislocations generate complex stress fields that, according to elastic mechanics theory [30–32], lower diffusion barriers and create preferential sites for vacancy aggregation. Direct evidence of clustering is provided by AC-STEM atomic-resolution images (Figs. 5(a) and 5(b)), which show distinct regions with local strain contrast (region A) adjacent to well-ordered domains (region B). Line-intensity profiles (Figs. 5(c) and 5(d)) further confirm the nonuniform atomic arrangements characteristic of vacancy-rich clusters. The cluster size within a unit cell and the associated lattice deformation, as derived from first-principles DFT calculations, are visualized in Figs. S3 and S4 in the ESM. In contrast, LC displays only randomly distributed point defects without clustering (Fig. 4(b)).

The driving forces for clustering are twofold (Fig. 6): (i) Local compressive strain from the smaller Sm^{3+} shortens the Sm–vacancy distance; (ii) Higher ionic potential of Sm^{3+} (2.78 vs. 2.59 for La^{3+}) polarizes electron clouds, creating electrostatic attraction toward positively charged oxygen vacancies. DFT calculations support this mechanism: the oxygen vacancy formation energy decreases from 4.19 eV in LC to 1.71 eV in $(La_{0.8}Sm_{0.2})_2Ce_2O_7$, lowering the energy barrier for aggregation without altering the total vacancy concentration. In LC, random free vacancies induce contraction through vacancy-phonon coupling (weakening lattice vibration anharmonicity) and local symmetry breaking (disrupting the cation coordination environment) [13]. Clustering reduces the number of mobile free vacancies, thereby weakening vacancy–phonon coupling and restoring local symmetry. This dual effect ultimately suppresses the low-temperature contraction.

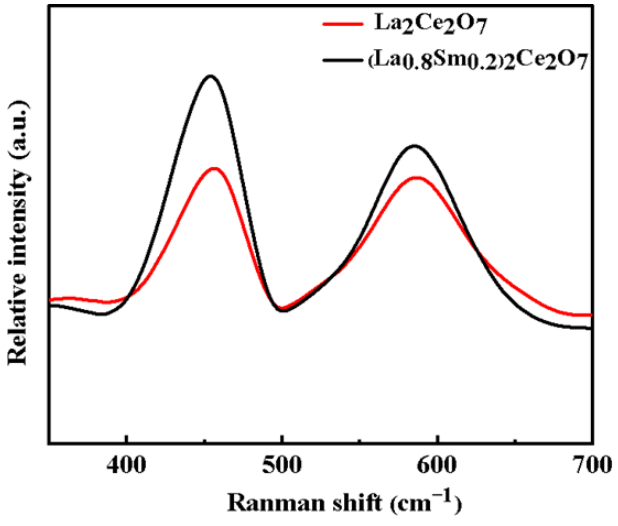

Fig. 3 Raman spectra of $(La_{1-x}Sm_x)_2Ce_2O_7$ ($x = 0$, 0.2) bulks.

3.6 Comparison with high-valent cation substitution

High-valent substitutions (e.g., Ta^{5+}) suppress contraction primarily by reducing the total vacancy concentration via charge compensation [14–16]. In contrast, Sm^{3+} isovalent substitution achieves contraction suppression by regulating vacancy distribution (clustering immobilizes free vacancies) without changing the total vacancy content. The two strategies are complementary, together expanding the LC's performance optimization theoretical system. Direct comparative experiments are unnecessary here, as high-valent substitution mechanisms are well documented [14–16,27], and the present work isolates "distribution" as the sole variable via combined DFT calculations and HR-TEM/AC-STEM evidence.

4 Conclusions

Sm^{3+} isovalent substitution in LC induces oxygen vacancy clustering, which nearly eliminates low-temperature contraction and increases the average TEC. This work confirms that LC's thermal expansion is coregulated by the oxygen vacancy concentration and distribution—An innovative mechanism

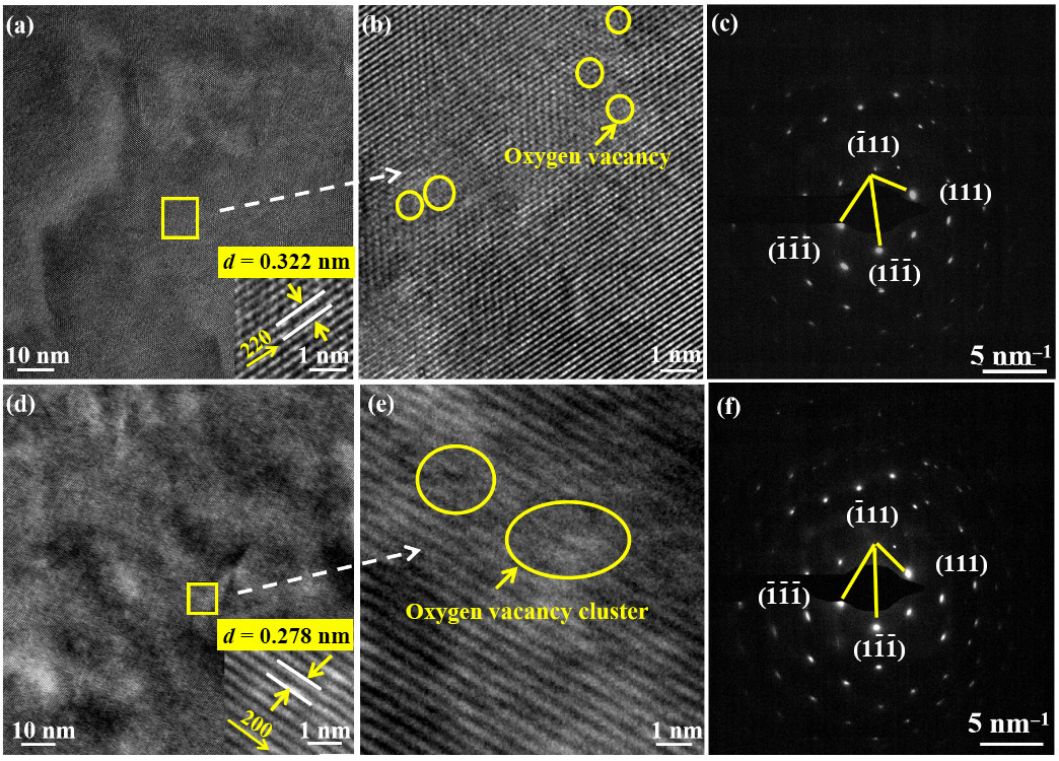

Fig. 4 Representative HR-TEM images and the corresponding selected area electron diffraction (SAED) patterns: (a–c) LC; (d–f) $(La_{0.8}Sm_{0.2})_2Ce_2O_7$.

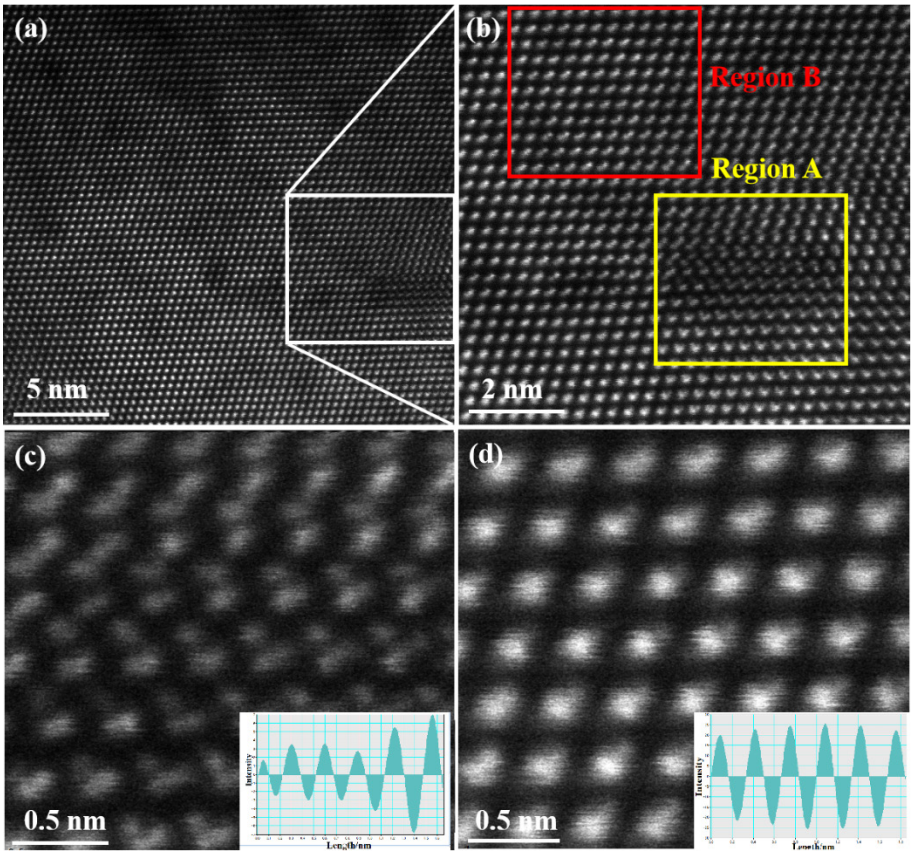

Fig. 5 AC-STEM images of $(La_{0.8}Sm_{0.2})_2Ce_2O_7$ bulk: (a) low-magnification view; (b) high-magnification image of the white region in (a), where regions A and B correspond to distinct atomic packing domains; (c) magnified view of region A, with the intensity profile reflecting the characteristics of atomic columns in this area (inset); (d) magnified view of region B, with the intensity profile demonstrating the periodicity of atomic columns in this area (inset).

complementing existing high-valent substitution strategies. The clustering is driven by synergistic local compressive strain and electrostatic attraction, as supported by DFT calculations and AC-STEM atomic-resolution evidence.

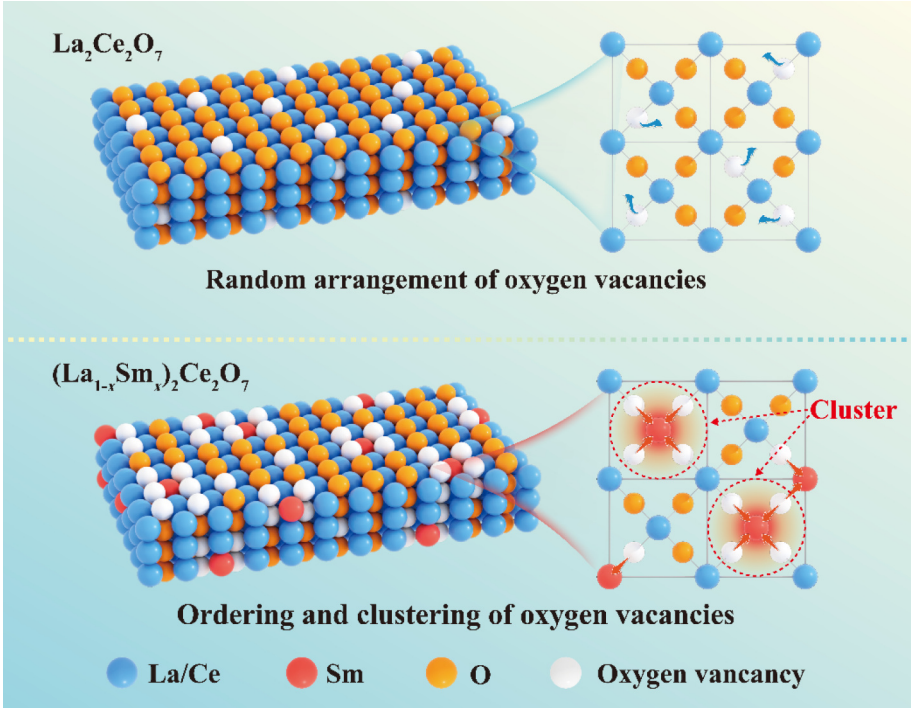

Fig. 6 Mechanism diagram of oxygen vacancy clustering.

The generalizability of the strategy relies on three criteria: identical valence to the host cation, high thermal stability, and moderate cation radius mismatch. Preliminary results with Gd_2O_3 and Nd_2O_3 indicate similar effectiveness. Future work will explore doping limits, additional thermophysical properties (e.g., thermal conductivity, elastic modulus) and long-term cycling performance. These findings provide a new pathway for designing high-performance TBC materials.

Acknowledgements

This work was financially supported by the National Natural Science Foundation of China (No. 52262006), Natural Science Foundation of Jiangxi Province (No. 20232BAB204018), Doctoral Start-up Fund Project of Jiangxi Science and Technology Normal University (No. 2020BSQD011), and Student Innovative Project of Jiangxi Science and Technology Normal University (No. YC2024-X16).

The authors gratefully acknowledge Dr. Fenning Zhao (Xinyu University, Xinyu 338004, Jiangxi, China) for guidance on modeling and structural optimization.

Availability of data and materials

The data that support the findings of this study are available from the corresponding author upon reasonable request.

Competing interests

The authors have no competing interests to declare that are relevant to the content of this article.

Electronic Supplementary Material

Supplementary material is available in the online version of this article at https://doi.org/10.26599/JAC.2026.9221245.

References

[1] Padture NP. Advanced structural ceramics in aerospace propulsion. *Nat Mater* 2016, **15**: 804–809.

[2] Chen L, Wang JK, Li BH, *et al.* Simultaneous manipulations of thermal expansion and conductivity in symbiotic $ScTaO_4/SmTaO_4$ composites via multiscale effects. *J Adv Ceram* 2023, **12**: 1625–1640.

[3] Zhao KR, Huang WZ, Deng PH, *et al.* Mechanical properties, thermal shock resistance and stress evolution of plasma-sprayed 56 wt% Y_2O_3-stabilized ZrO_2 thick thermal barrier coatings. *Surf Coat Tech* 2024, **494**: 131352.

[4] Guo L, Li YY, Yan K. Corrosion behavior of $Gd_2Zr_2O_7$ thermal barrier coatings under Fe-containing environmental sediment attack. *J Adv Ceram* 2024, **13**: 447–462.

[5] Sezavar A, Sajjadi SA. A review on the performance and lifetime improvement of thermal barrier coatings. *J Eur Ceram Soc* 2025, **45**: 117274.

[6] Chen XL, Chen L, Tian J, *et al.* Measurements and applications of thermal–mechanical properties of thermal/environmental barrier coating materials. *Adv Ceram* 2025, **46**: 389–415

[7] Chen XG, Zhang HM, Zhang HS, *et al.* $Ce_{1-x}Sm_xO_{2-x/2}$—A novel type of ceramic material for thermal barrier coatings. *J Adv Ceram* 2016, **5**: 244–252.

[8] Chen L, Li BH, Feng J. Rare-earth tantalates for next-generation thermal barrier coatings. *Prog Mater Sci* 2024, **144**: 101265.

[9] Zou BL, Zhang YQ, Wang Y, *et al.* Microwave-absorbing functionalization of $LaMgAl_{11}O_{19}$ composite thermal barrier coatings by atmospheric plasma spraying. *J Adv Ceram* 2024, **13**: 1523–1534.

[10] Huang WZ, Zhong RQ, Zhou X, *et al.* Degradation of $LaPO_4$–8YSZ composite thick thermal barrier coatings by molten calcium–magnesium–aluminosilicate. *J Eur Ceram Soc* 2025, **45**: 116863.

[11] Zou LX, Cheng YX, Meng SJ, *et al.* Construction of a molten CMAS-resistant bilayer-structured apatite layer used for thermal barrier coatings. *J Adv Ceram* 2025, **14**: 9221173.

[12] Chen XG, Zhang XP, Xue YF, *et al.* Investigation of thermophysical properties and elastic moduli of $Sm_2GdTa_{1-x}Ce_xO_{7-x/2}$ oxides for thermal barrier coatings. *Ceram Int* 2025, **51**: 27550–27556.

[13] Cao XQ, Vassen R, Fischer W, *et al.* Lanthanum–cerium oxide as a thermal barrier-coating material for high-temperature applications. *Adv Mater* 2003, **15**: 1438–1442.

[14] Ma W, Gong SK, Xu HB, *et al.* On improving the phase stability and thermal expansion coefficients of lanthanum cerium oxide solid solutions. *Scripta Mater* 2006, **54**: 1505–1508.

[15] Zhang H, Sun JB, Duo SW, *et al.* Thermal and mechanical properties of Ta_2O_5 doped $La_2Ce_2O_7$ thermal barrier coatings prepared by atmospheric plasma spraying. *J Eur Ceram Soc* 2019, **39**: 2379–2388.
[16] Zhang H, Wang JS, Dong SJ, *et al.* Mechanical properties and thermal cycling behavior of Ta_2O_5 doped $La_2Ce_2O_7$ thermal barrier coatings prepared by atmospheric plasma spraying. *J Alloys Compd* 2019, **785**: 1068–1076.
[17] Zhang HS, Chen XG, Li G, *et al.* Influence of Gd_2O_3 addition on thermophysical properties of $La_2Ce_2O_7$ ceramics for thermal barrier coatings. *J Eur Ceram Soc* 2012, **32**: 3693–3700.
[18] Shi MG, Ma SY, Xia WS, *et al.* Effects of oxygen vacancy on bond ionicity, lattice energy, and microwave dielectric properties of CeO_2 ceramics with Yb^{3+} substitution. *J Adv Ceram* 2024, **13**: 247–254.
[19] Lin YL, Zou LX, Dai JW, *et al.* First-principles application in the research field of thermal barrier coating. *Adv Ceram* 2025, **46**: 24–51
[20] Liu BS, Zhao JL, Chu KL, *et al.* Unraveling the atomic-scale mechanisms of hydrogen defects behavior in yttria-stabilized tetragonal zirconia by first principles calculation. *J Adv Ceram* 2025, **14**: 9221099.
[21] Lin YL, Yang Y, Dai JW, *et al.* High-entropy strategy makes rare-earth phosphates more suitable for use as thermal barrier coating materials. *Ceram Int* 2025, **51**: 59120–59129.
[22] Gao ZX, Fu S, Zhang L, *et al.* Thermodynamic characterization of $RE_2Ti_2O_7$ (RE = Ho, Er, Tm and Yb) ceramics as thermal barrier coating materials. *Mater Today Phys* 2025, **57**: 101801.
[23] Zhang HS, Lv JG, Li G, *et al.* Preparation, characterization, and thermophysical properties of $(La_{0.95}Sr_{0.05})_2Ce_2O_{6.95}$ ceramic for thermal barrier coatings. *Int J Appl Ceram Technol* 2014, **11**: 350–358.
[24] Zhang HS, Wei Y, Li G, *et al.* Investigation about thermal conductivities of $La_2Ce_2O_7$ doped with calcium or magnesium for thermal barrier coatings. *J Alloys Compd* 2012, **537**: 141–146.
[25] Shannon RD. Revised effective ionic radii and systematic studies of interatomic distances in halides and chalcogenides. *Acta Crystallogr A* 1976, **32**: 751–767.
[26] Zhang HS, Sun K, Xu Q, *et al.* Thermal conductivity of $(Sm_{1-x}La_x)_2Zr_2O_7$ (x = 0, 0.25, 0.5, 0.75 and 1) oxides for advanced thermal barrier coatings. *J Rare Earths* 2009, **27**: 222–226.
[27] Zhang H, Zeng JY, Yuan JY, *et al.* Spray power-governed microstructure and composition, and their effects on properties of lanthanum–cerium–tantalum-oxide thermal barrier coating. *Ceram Int* 2020, **46**: 18114–18122.
[28] Zhang Y, Guo L, Zhao XX, *et al.* Toughening effect of Yb_2O_3 stabilized ZrO_2 doped in $Gd_2Zr_2O_7$ ceramic for thermal barrier coatings. *Mat Sci Eng A* 2015, **648**: 385–391.
[29] Guo L, Zhang CL, Xu LM, *et al.* Effects of TiO_2 doping on the defect chemistry and thermo–physical properties of Yb_2O_3 stabilized ZrO_2. *J Eur Ceram Soc* 2017, **37**: 4163–4169.
[30] Duhan N, Patil RU, Mishra BK, *et al.* Thermo–elastic analysis of edge dislocation using extended finite element method. *Int J Mech Sci* 2021, **192**: 106109.
[31] Zhao Y, Zhu YM, Zhu JP, *et al.* Atomic-resolution investigation of structural transformation caused by oxygen vacancy in $La_{0.9}Sr_{0.1}TiO_{3+\delta}$ titanate layer perovskite ceramics. *J Mater Sci Technol* 2022, **104**: 172–182.
[32] Duhan N, Patil RU, Mishra BK, *et al.* Nonlinear thermo–elastic analysis of edge dislocations with internal heat generation in semiconductor materials. *Mech Mater* 2022, **169**: 104322.